Eur. Phys. J. Special Topics **225**, 343–354 (2016)

DOI: 10.1140/epjst/e2016-02636-5

THE EUROPEAN PHYSICAL JOURNAL SPECIAL TOPICS

Regular Article

The response of polymethyl methacrylate (PMMA) subjected to large strains, high strain rates, high pressures, a range in temperatures, and variations in the intermediate principal stress

T.J. Holmquist[1,a], J. Bradley[2], A. Dwivedi[2], and D. Casem[2]

[1] Southwest Research Institute, Minneapolis, MN 55416, USA
[2] US Army Research Laboratory, Aberdeen Proving Ground, MD 21005, USA

Received 26 August 2015 / Received in final form 12 February 2016
Published online 14 March 2016

Abstract. This article presents the response of polymethyl methacrylate (PMMA) subjected to large strains, high strain rates, high pressures, a range in temperatures, and variations in the intermediate principal stress. Laboratory data from the literature, and new test data provided here, are used in the evaluation. The new data include uniaxial stress compression tests (at various strain rates and temperatures) and uniaxial stress tension tests (at low strain rates and ambient temperatures). The compression tests include experiments at $\dot{\varepsilon} = 13,000\,\mathrm{s}^{-1}$, significantly extending the range of known strain rate data. The observed behavior of PMMA includes the following: it is brittle in compression at high rates, and brittle in tension at all rates; strength is dependent on the pressure, strain, strain rate, temperature, and the intermediate principal stress; the shear modulus increases as the pressure increases; and it is highly compressible. Also presented are novel, high velocity impact tests (using high-speed imaging) that provide insight into the initiation and evolution of damage. Lastly, computational constitutive models for pressure, strength, and failure are presented that provide responses that are in good agreement with the laboratory data. The models are used to compute several ballistic impact events for which experimental data are available.

1 Introduction

Polymethyl methacrylate (PMMA) is a light-weight, transparent, plastic often used as a substitute for glass in products such as shatterproof windows and protective eyewear. It is also commonly used as a backing (window) material in plate-impact experiments. Because of these various applications there is interest in understanding (and modeling) its behavior subjected to the conditions associated with high

[a] e-mail: timothy.holmquist@swri.org

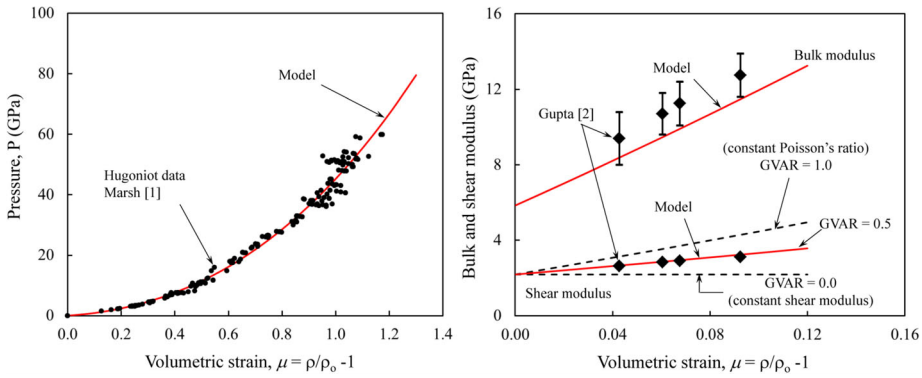

Fig. 1. The pressure (left), bulk modulus and shear modulus (right) vs. volumetric strain.

velocity impact. Thus, the primary objective of this work is to provide an overall understanding of the behavior of PMMA for which material models can be developed and validated. Test data from the literature, and new data presented here, are used in the evaluation. A secondary objective is to present a material model (for pressure, strength and failure) that captures the complex responses exhibited by the data. The remainder of this article presents a discussion of the experimental data, a description of the material models, computed results, and a summary and conclusion.

2 Experimental data

The following subsections present detailed discussions of the pressure-volume response, the flow stress response, and the failure response of PMMA. Much of the data are from the literature, but data from the present work are also included. The new data presented here are for Plexiglas G produced by Arkema of Altuglas International. Although the test data from the literature are from many different sources, it will be shown that their responses (including the data provided here) are all very similar. It should be noted that most of the figures that present experimental data also include the response of the models. The models will be discussed following the discussion of the test data.

2.1 Pressure

The pressure-volume response of PMMA is presented in Fig. 1 and the data are provided by Marsh [1] and Gupta [2]. The density is $\rho_o = 1186\,\mathrm{kg/m^3}$, the shear modulus is G = 2.19 GPa, and the bulk modulus is K = 5.85 GPa as provided by Marsh [1]. The material is very compressible, e.g., the density doubles at a pressure of 45 GPa. It also exhibits a shear modulus that increases as the volumetric strain increases as identified by Gupta [2], reproduced on the right side of Fig. 1. The shear modulus increases at a rate approximately half that produced by a constant Poissons ratio.

2.2 Strength

The strength of PMMA is complex, and is a function of strain, strain rate, temperature, pressure and the intermediate principal stress. There are significant amounts

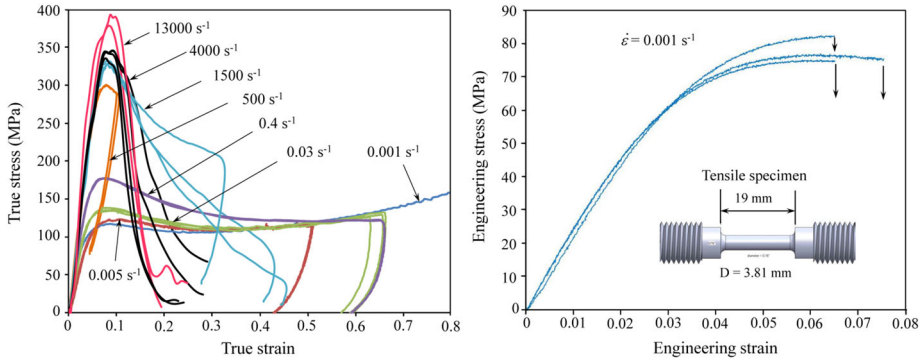

Fig. 2. The stress-strain responses in compression for many different strain rates (left), and for tension at a quasistatic strain rate (right).

of test data available in the literature which are used in this subsection, as well as some new data generated by the authors. Figure 2 presents uniaxial stress compression data for strain rates ranging from $\dot{\varepsilon} = 0.001\,\mathrm{s}^{-1} - 13,000\,\mathrm{s}^{-1}$ and for tension tests at $\dot{\varepsilon} = 0.001\,\mathrm{s}^{-1}$. The lower rate compression tests used right circular cylinders, 5 mm in diameter and 5 mm thick. Smaller specimens were used for the very high rate tests (2.5 mm in diameter and 2.5 mm thick). The tensile specimens used a gauge length of 19 mm and a gage diameter of 3.81 mm and were pulled to failure. Several observations are made from the test results presented in Fig. 2: the onset of permanent deformation (yielding) appears to occur at approximately the peak stress (a true strain of approximately 0.08); adiabatic heating begins to soften the responses at a strain rate of $0.03\,\mathrm{s}^{-1}$; the strength is very rate sensitive increasing by nearly 4x over the strain rates presented; in compression the material transitions from a very ductile response to a very brittle response between a strain rate of $1500\,\mathrm{s}^{-1}$ and $4000\,\mathrm{s}^{-1}$ (the material did not fail when the strain rate was $1500\,\mathrm{s}^{-1}$ and below, but failed in a catastrophic, brittle manner at strain rates of $4000\,\mathrm{s}^{-1}$ and $13,000\,\mathrm{s}^{-1}$); in tension the yield stress is lower than compression and it is brittle (little or no plastic deformation at failure). The compression data presented by Nasraoui et al. [3] (for $0.001\,\mathrm{s}^{-1} \leq \dot{\varepsilon} \leq 3335\,\mathrm{s}^{-1}$) are in good agreement with the data presented here. It should be noted that the tests at $\dot{\varepsilon} = 13,000\,\mathrm{s}^{-1}$ significantly extend the range of known strain rate data, and exhibit a continued increase in peak strength. It should also be noted that PMMA has a low thermal diffusivity resulting in thermal softening at strain rates greater than $0.01\,\mathrm{s}^{-1}$ [3].

The effect of temperature is presented in Fig. 3. The left portion presents compression stress-strain responses for initial temperatures of 295 K (room), 311 K, 327 K and 344 K. The right portion presents normalized yield stress as a function of homologous temperature for several sets of data. The data are provided by Nasraoui et al. [3], Quinson et al. [4] and the present work. Although there are four sets of data, from three different sources, the responses are very consistent. Note that the glass transition temperature is 398 K [5] and is taken here as the melting temperature (the temperature where the yield stress goes to zero, $T^* = 1.0$). Also note that because there are low temperature data provided by Nasraoui et al. [3], T_{ref} is taken as 213 K which results in $T^* = 0.44$ equaling room temperature (295 K).

Figure 4 presents the effect of strain rate and pressure on the yield stress. The left side shows compressive yield stress as a function of strain rate and the data are provided by Nasraoui et al. [3], Blumenthal et al. [6], Li and Lambros [7], Mulliken and Boyce [8], Richeton et al. [9], Moy et al. [10], Rittel and Brill [11], and the present work. The rate effect on the yield stress is dramatic, increasing from approximately

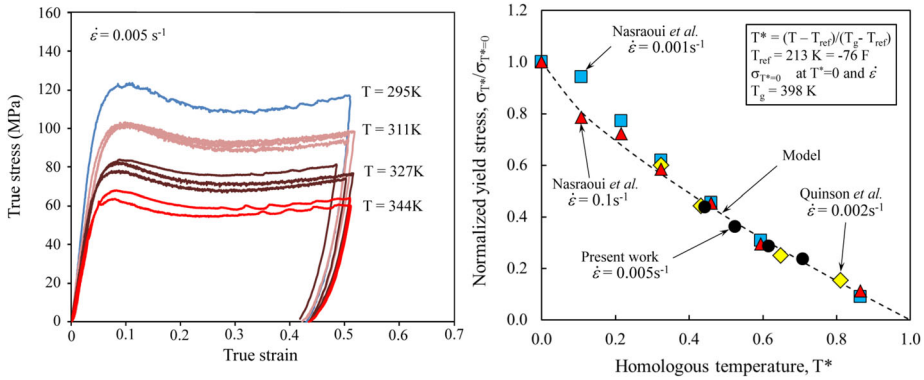

Fig. 3. The stress-strain responses in compression for initial temperatures of 295 K, 311 K, 327 K and 344 K (left). The right shows normalized yield stress vs. homologous temperature.

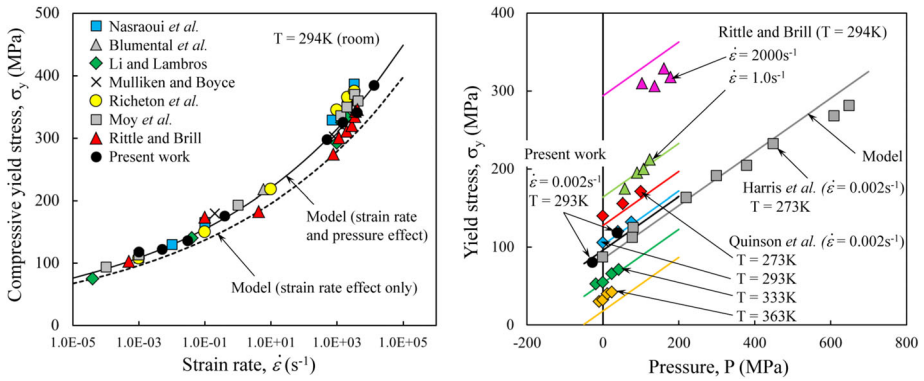

Fig. 4. The left side presents the compressive yield stress as a function of strain rate and the right side presents yield stress as a function of pressure.

100 MPa to 400 MPa over 8 orders of magnitude in strain rate. It should be noted that a small portion of this increase is due to pressure hardening. Also note that although the data are from eight different sources, they are very consistent.

The right side of Fig. 4 presents yield stress as a function of pressure, for different strain rates, temperatures, and stress states. The data are provided by Rittel and Brill [11], Harris et al. [12], Quinson et al. [4], and the present work. The yield stress increases significantly as the pressure increases. It appears that this pressure hardening effect is independent of temperature, strain rate, and the stress state (torsion) because the slopes are all similar.

Lastly, the effect of the intermediate principal stress is discussed (often referred to as the third-invariant effect). Figure 5 presents the equivalent stress as a function of plastic strain for a compression test provided by Nasraoui et al. [3] and the present work, and a torsion test provided by Fleck et al. [5]. The tests were performed at ambient temperature and an equivalent strain rate of $\dot{\varepsilon} = 0.001\,\mathrm{s}^{-1}$. The torsion test was converted to equivalent stress and equivalent plastic strain using the standard relationships $\sigma = \sqrt{3}\tau$ and $\varepsilon_p = \gamma_p/\sqrt{3}$ respectively, where τ is the shear stress and γ_p is the plastic shear strain. In uniaxial stress compression the intermediate principal stress is $\sigma_{II} = 0$ (where $\sigma_I < \sigma_{II} = \sigma_{III} = 0$); this stress state lies on the compressive meridian. In torsion the intermediate principal stress is also $\sigma_{II} = 0$ but lies midway between σ_I and σ_{III} (where $\sigma_I = -\sigma_{III}$); this stress state is midway

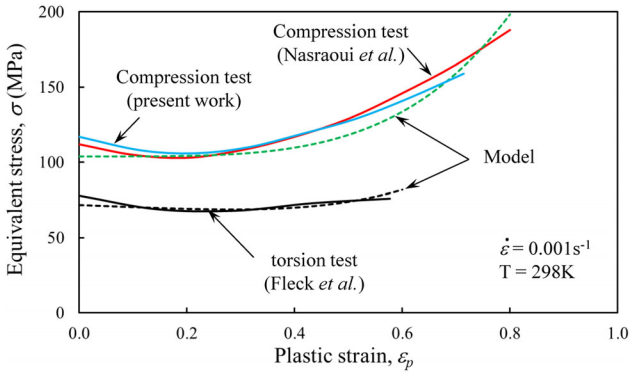

Fig. 5. Equivalent stress as a function of plastic strain for two compression tests and a torsion test.

between the tensile and compressive meridian. As shown in Fig. 5 the flow stress in torsion is significantly lower than that produced under uniaxial stress compression. Approximately a third of this difference is due to pressure hardening (inferred from Fig. 4) and the remaining difference is due to the effect of the intermediate principal stress.

2.3 Failure

Figure 6 presents the plastic failure strain as a function of the pressure-stress ratio, $\sigma^* = -P/\sigma$, and strain rate, where P is the hydrostatic pressure (positive in compression) and σ is the equivalent stress. The data are provided by Fleck et al. [5], Nasraoui et al. [3], Wu et al. [13], Barker and Hollenbach [14], and the present work. A single symbol indicates failure at the designated strain. A single symbol with a dashed line and arrow indicates that the test was stopped at the indicated strain and there was no failure. Two symbols, connected by a dashed line, indicate failure, but it is not known at what plastic strain failure occurred. The test data exhibit several interesting failure characteristics: PMMA is very brittle in tension at all strain rates, it is ductile in compression at rates below $1500\,\mathrm{s}^{-1}$ and transitions to brittle behavior somewhere between $1500\,\mathrm{s}^{-1}$ and $4000\,\mathrm{s}^{-1}$, and failure is very sensitive to the pressure-stress ratio. In the present work, when failure did occur, it was brittle and catastrophic. It is not clear what mechanisms are responsible for the ductile to brittle transition that occurs at elevated strain rates, but it appears to be a real material characteristic as it has been observed by several other researchers [3,6,10,11].

2.4 High velocity impact experiments

High velocity impact experiments were performed to provide insight into damage initiation, propagation and failure of PMMA; and to provide validation experiments for material models. Two configurations were used: a Taylor bar test and a punch test. The Taylor bar experiment consisted of a PMMA cylinder, 25.4 mm long and 6.35 mm in diameter. The Taylor bars impacted a long steel anvil, 12.7 mm in diameter, at two different impact velocities, and the impact responses were captured using high speed imaging. Figure 7 presents the result for an impact velocity of V = 113 m/s. High speed photographs are presented at t = 0, 8, 16, 32, 40 and 48 μs after impact. In all the images the full Taylor bar is visible including the front portion of the steel anvil.

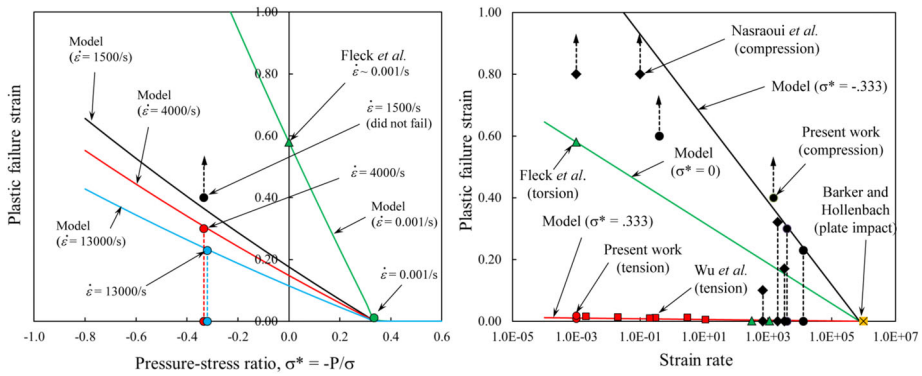

Fig. 6. Plastic failure strain vs. the pressure-stress ratio (left) and the strain rate (right).

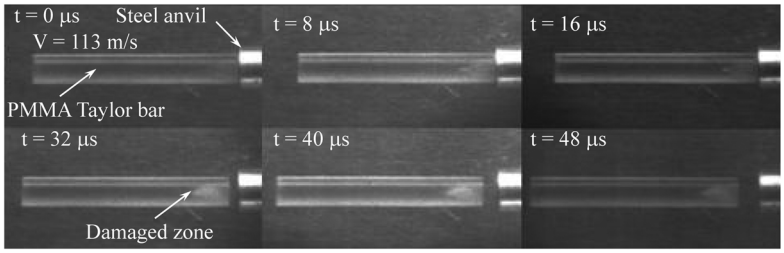

Fig. 7. Experimental result from the V = 113 m/s Taylor bar experiment. Images are presented at t = 0, 8, 16, 32, 40 and 48 μs after impact.

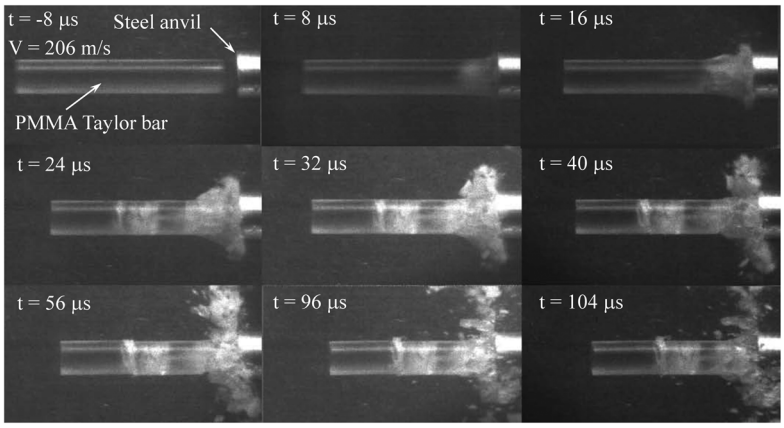

Fig. 8. Experimental result from the V = 206 m/s Taylor bar experiment. Images are presented at t = −8, 8, 16, 24, 32, 40, 56, 96 and 104 μs after impact.

Target impact occurs at the image marked by t = 0 μs and begins to rebound sometime before t = 32 μs. The bar remains intact, but there is evidence of damage near the front as inferred by the zone of opaqueness. Figure 8 presents the experimental result for an impact velocity of V = 206 m/s with images shown at t =−8, 8, 16, 24, 32, 40, 56, 96 and 104 μs after impact. The front of the rod is shattered into many small fragments and a late time failure (probably tension) occurs toward the rear of the bar, sometime between t = 16 and 24 μs after impact.

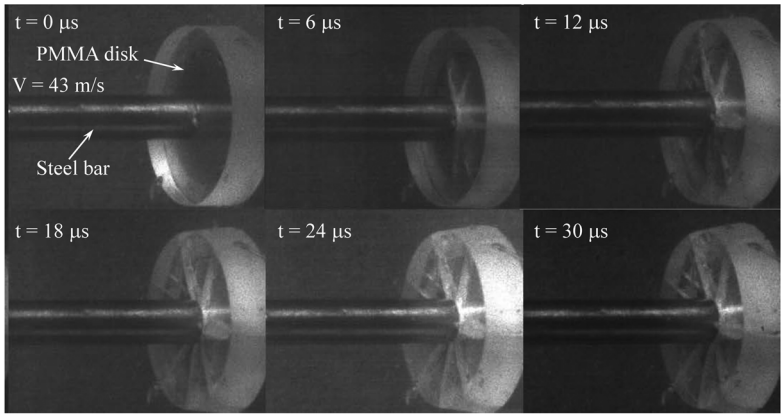

Fig. 9. Experimental result from the V = 43 m/s punch test. Images are presented at t = 0, 6, 12, 18, 24 and 30 μs after impact. Approximately eight radial cracks are formed.

The punch test consists of a PMMA disk, 25.4 mm in diameter and 6.35 mm thick. The disk is supported by a steel cylinder having an outer diameter of 25.4 mm and an inner diameter of 19.17 mm. A steel rod, 6.33 mm in diameter and 50 mm long, impacts the PMMA disk. High speed imaging is used to capture the response. Two impact velocities are discussed, one at V = 43 m/s and the other at V = 83 m/s. Figure 9 presents the results from the V = 43 m/s impact condition and images are shown at t = 0, 6, 12, 18, 24 and 30 μs after impact. At t = 6 μs several radial cracks are evident but have not propagated to the outer edge of the disk. At t = 18 μs it appears that all the radial cracks have completely formed and are fully extended to the perimeter. At t = 24, and 30 μs it appears that no additional cracks are formed (there are approximately eight) and the motion appears rigid body (the pie shaped pieces are being separated). The result from the V = 83 m/s impact condition was very similar to that of the V = 43 m/s test other then there appeared to be more radial cracks formed (approximately ten).

3 Description of the models

The authors are aware that there are several sophisticated models for PMMA available in the literature [8,15,16]. A characteristic of these models is their formulations are physically based providing a more physical representation of the material response. However, they are complex, can be difficult to incorporate into computer codes, and it is not clear how robust, efficient and accurate they are for computing high velocity impact events. Alternatively, phenomenological models are not physically based, but they can be readily incorporated into computer codes, and can be robust and efficient. The objective of this section is to demonstrate that with the appropriate formulation, phenomenological models can accurately represent the response of PMMA, and possibly other polymers. The following presents a description of the models for pressure, strength, and failure used to describe the behavior of PMMA.

The Mie-Gruneisen equation of state is used to describe the pressure as a function of volumetric strain and internal energy and is expressed as

$$P = P_H(1 - \Gamma\mu/2) + \Gamma E_s(1 + \mu) \tag{1}$$

where $\mu = \rho/\rho_o - 1$, ρ_o is the initial density, ρ is the current density, Γ is the Gruneisen coefficient, E_s is the internal energy per initial volume and P_H is the

Hugoniot expressed as

$$P_H = K_1\mu + K_2\mu^2 + K_3\mu^3 \tag{2}$$

where K_1 is the bulk modulus, and K_2 and K_3 are constants. Figure 1 presents the Hugoniot data provided by Marsh [1] and a fit to the data using Eq. (2). The model provides a response that is in good agreement with the data.

A characteristic of PMMA is that the shear modulus increases as the volumetric strain (or pressure) increases, as shown on the right side of Fig. 1. The test data are represented by the black diamonds [2] and show both the bulk modulus and the shear modulus increasing with increasing volumetric strain. The models are shown with red lines. The bulk modulus, $K(\mu)$, is simply the derivative of the pressure response from Fig. 1 (left) and provides a response that is at the low end of the data. The shear modulus is described by a feature that interpolates between a response defined by a constant shear modulus (GVAR = 0), and a constant Poissons ratio (GVAR = 1.0), using the interpolation factor, GVAR. GVAR = 0.5 provides a response that is in good agreement with the data.

In 1991 Holmquist and Johnson [17] presented a modification to the original JC strength model [18] that provides an enhanced strain rate effect at high strain rates. An exponential function, instead of a linear function of the natural log, is used. This modified JC model is expressed as

$$\sigma = [A + B\varepsilon^n][\dot{\varepsilon}^{*C_3}][1 - T^{*M}] + C_4P \tag{3}$$

where ε is the equivalent plastic strain, $\dot{\varepsilon}^* = \dot{\varepsilon}/\dot{\varepsilon}_o$ is the dimensionless total strain rate for $\dot{\varepsilon}_o = 1.0s^{-1}$, $T^* = (T - T_{ref})/(T_M - T_{ref})$ is the homologous temperature where T_{ref} is the reference temperature, T_M is the melt temperature and T is the actual temperature, and P is the pressure (compression is positive). This model also includes a pressure component as presented by Johnson et al. [19]. The constants are A, B, n, C_3, M and C_4 and are determined using the test data from Figs. 3–5, and a procedure similar to that described by Johnson and Cook [18]. This model is used to describe the strength of PMMA because it more accurately represents the strain rate effect and includes the effect of pressure. It should be noted that the effect of the third invariant is also included. A discussion of its implementation is provided by Johnson et al. [20]. This model provides a response that is in good agreement with high and low temperature data (Fig. 3), strain rate and high pressure data (Fig. 4), and third invariant data (Fig. 5).

The Johnson-Cook failure model [21] is used to describe the failure response of PMMA and is expressed as

$$\varepsilon_p^f = [D_1 + D_2 exp(D_3\sigma^*)][1 + D_4 ln\dot{\varepsilon}^*][1 + D_5T^*] \tag{4}$$

where ε_p^f is the equivalent plastic failure strain under constant conditions of the dimensionless total strain rate, $\dot{\varepsilon}^*$, homologous temperature, T^*, and the pressure-stress ratio, $\sigma^* = -P/\sigma$. The constants are D_1, D_2, D_3, D_4 and D_5 and are determined using the test data from Fig. 6 and the standard procedure described by Johnson and Cook [21]. This model is used because it provides a good representation of the observed failure behavior of PMMA.

Figure 6 (left) presents plastic failure strain as a function of the pressure-stress ratio for both the model and test data. Quasistatic tension data and high rate compression data are shown including quasistatic torsion data provided by Fleck et al. [5]. The compression test at $\dot{\varepsilon} = 1500\,\mathrm{s}^{-1}$ is shown with an upward arrow because it did not fail; the data at $\dot{\varepsilon} = 4000\,\mathrm{s}^{-1}$ and $13,000\,\mathrm{s}^{-1}$ failed catastrophically (into many small fragments) and are shown over the strains observed in the experiment because it is not known at what strain failure occurred. The model is shown for a strain rate

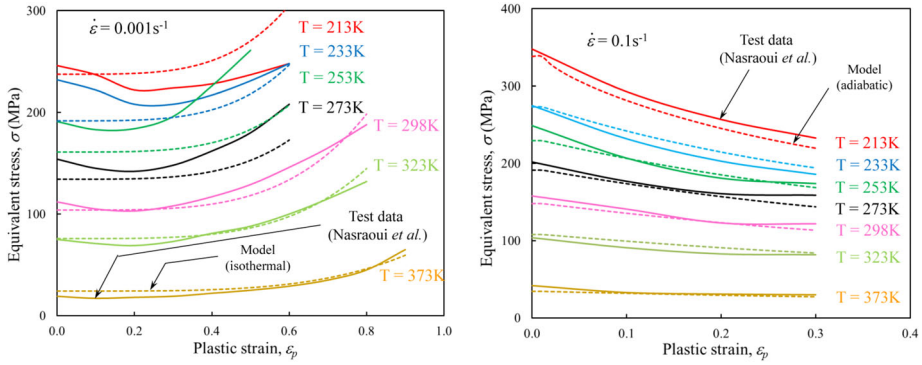

Fig. 10. A comparison between the computed and experimental stress-strain responses for different initial temperatures. The left is for a strain rate of $0.001\,\mathrm{s}^{-1}$ where the responses are isothermal, the right is for a strain rate of $0.1\,\mathrm{s}^{-1}$ where the responses are adiabatic.

of $0.001, 1500, 4000$ and $13,000\,\mathrm{s}^{-1}$, and is generally in good agreement with the test data.

Figure 6 (right) presents plastic failure strain as a function of strain rate for several experiments and the model. The tension data (shown in red) are brittle at all strain rates, the torsion data (shown in green) show decreased ductility with increasing strain rates, and the compression data (shown in black) show a strong dependence on strain rate. The model is shown at a $\sigma^* = -0.333$ (compression-black), $\sigma^* = 0$ (torsion-green), and $\sigma^* = 0.333$ (tension-red), and is generally in good agreement with the test data.

4 Computed results

This section presents computed results for some of the laboratory tests and for several ballistic impact experiments. The model was compared to many of the laboratory tests in the previous section where the yield stress was evaluated as a function of strain rate, temperature and pressure. Here, the more complex flow stress responses are presented as a function of strain rate and temperature. The ballistic experiments used for validation include plate impact tests, Taylor bar tests, punch tests, and ballistic limit (V_{50}) tests. All the computations use the material models presented in the previous section, the same set of constants, and the 2013 version of the EPIC code.

Figure 10 compares the flow stress responses for many different initial temperatures. The left figure is for a strain rate of $0.001\,\mathrm{s}^{-1}$ (where the responses are isothermal) and the right figure is for a strain rate of $0.1\,\mathrm{s}^{-1}$ (where the responses are adiabatic). Figure 11 (left) compares the stress-strain responses for several strain rates where some of the responses are isothermal and some are adiabatic. The model is in good agreement with the laboratory data and provides a good test for the model because the flow stress response for various strain rates, temperatures and pressures is complex.

Figure 11 (right) compares the computed and experimental results for two plate impact configurations. The experiments are provided by Barker and Hollenbach [14]. Configuration 1 uses a 6.6 mm PMMA impactor, a 6.4 mm PMMA target, backed by a 25 mm PMMA window. Configuration 2 uses the same geometry except the impactor is replaced by fused silica. The impact velocity is V = 450 m/s for configuration 1 and V = 610 m/s for configuration 2. The computed results are in good

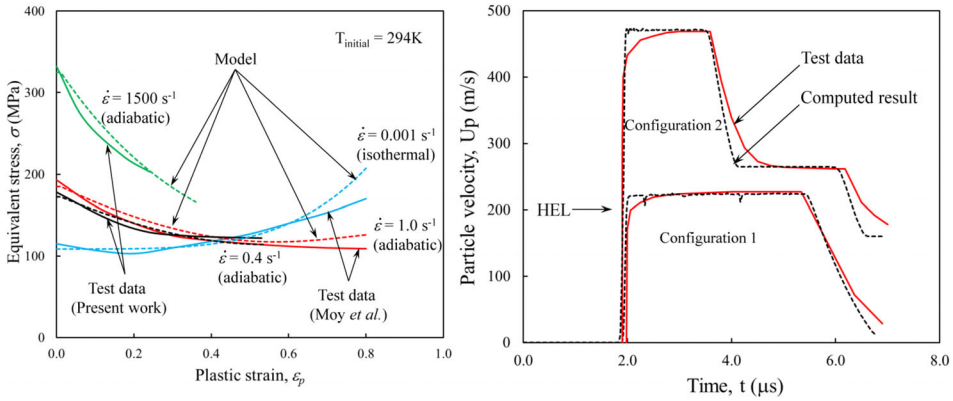

Fig. 11. The left portion compares the computed and experimental stress-strain responses for different strain rates. The right portion presents a comparison of the computed and experimental particle velocity-time histories for two plate impact configurations.

agreement with the experiments. A noteworthy characteristic, of both the tests and the computed results, is the lack of any HEL cusp in the particle velocity (Up) wave profiles. Barker and Hollenbach provide a significant discussion on this and offered several possible explanations. They concluded that the HEL = 700−800 MPa determined from a change in slope in the stress-strain Hugoniot response. This was also the conclusion of Gupta [2] where he identified softening to occur at 800 MPa, indicative of yielding. There is also no noticeable cusp in the computed results (which would be expected at approximately Up = 200 m/s) because the combination of pressure hardening, strain-rate hardening, and thermal softening provide a smooth transition from elastic to plastic behavior at the HEL (Up = 200 m/s).

Figure 12 presents a comparison of the computed and experimental Taylor bar results. The left side compares the V = 113 m/s impact where the computed result shows damage near the front similar to the experiment. There is also very little failed material (red) in the bar allowing it to stay intact and rebound off the anvil. The right side compares the results for the V = 206 m/s impact. The front of the rod is shattered into many small fragments for both the experiment and the computation. There is late time failure (away from the impact surface) that occurs in the test, but is not reproduced in the computed result, although a small amount of failure is computed about a diameter from the rear surface. The computed results are in good agreement with the experiments inasmuch as there is no failure at the low velocity and significant failure and fragmentation at the high velocity.

Figure 13 presents a comparison of the computed and experimental punch tests for V = 43 m/s and V = 83 m/s. The failure characteristics are very similar for both the computed and experimental results. Failure is brittle where the PMMA disk breaks into several pieces. At V = 43 m/s the experimental disk produces approximately eight radial cracks and approximately ten when the velocity is increased to V = 83 m/s. The computed results show a similar response producing six radial cracks at V = 43 m/s and eight at V = 83 m/s.

Figure 14 presents computed and experimental ballistic limit (V_{50}) results for PMMA plates impacted by a .22-cal fragment-simulanting projectile (FSP). The ballistic limit represents the impact velocity required to just perforate the PMMA plate. The test data are provided by Hsieh et al. [22], and Dehmer and Klusewitz [23]. The initial geometry, for both the experiments and the computations, include a 0.5-mm 2024-aluminum plate located behind the PMMA. The aluminum plate must

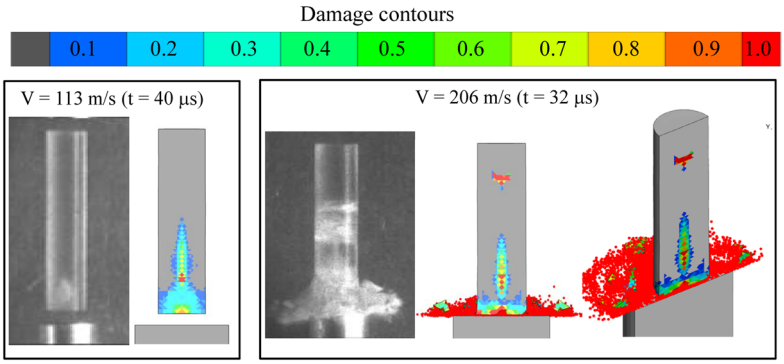

Fig. 12. A comparison of the computed and experimental results for the Taylor bar tests.

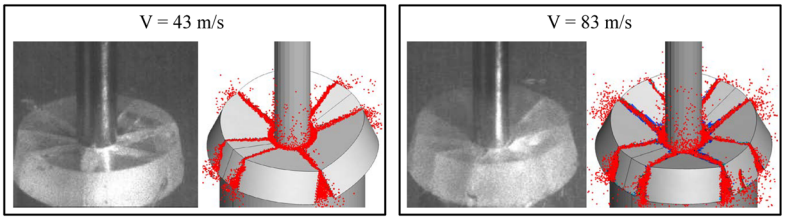

Fig. 13. A comparison of the computed and experimental results for the punch test.

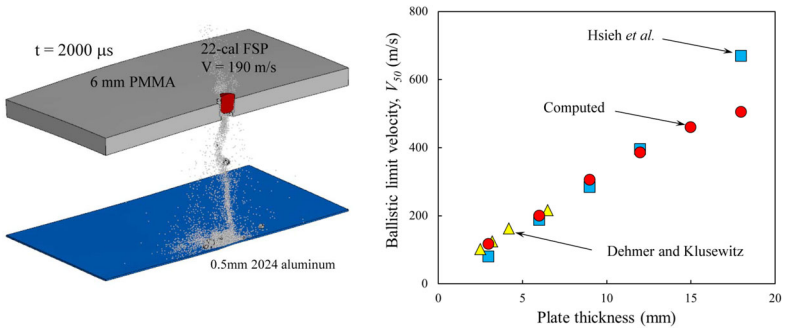

Fig. 14. Comparison of the computed and experimental ballistic limit velocities for various plate thicknesses of PMMA.

be perforated for the test to be deemed a perforation. An example of this is presented on the left side of Fig. 14 where the computed result is shown for a 6-mm PMMA plate impacted at V = 190 m/s. Although the FSP produces behind armor debris it does not perforate the aluminum plate and thus is not considered a perforation. The right side of Fig. 14 compares the computed and experimental results. The computed results are in good agreement for plate thicknesses up to 12 mm, but under-predicts the PMMA resistance for an 18 mm plate.

5 Summary and conclusions

This article has presented the response of polymethyl methacrylate (PMMA) subjected to large strains, high strain rates, high pressures, a range in temperatures, and variations in the intermediate principal stress. Laboratory data from the literature,

and new test data provided here, were used in the evaluation. The observed behavior included the following: it is brittle in compression at high rates, and brittle in tension at all rates; strength is dependent on the pressure, strain, strain rate, temperature, and the intermediate principal stress; yield stress is larger in compression and lower in tension; the shear modulus increases as the pressure increases; and the compressibility is large. A noteworthy observation was the consistency of the data; although the data were from many sources (most of unknown origin), their responses were remarkably similar. Also presented were novel, high velocity impact tests (using high-speed imaging) that provided insight into the initiation and evolution of damage. Computational constitutive models for pressure, strength, and failure were presented that provided responses that were in good agreement with the laboratory data. The models were also used to compute high velocity impact experiments which included plate-impact, Taylor bar, punch, and ballistic limit tests. The computed results were generally in good agreement with the experiments.

This work was performed for the U.S. Army Research Laboratory (ARL), Aberdeen Proving Ground, MD under contract No. W911QX-10-C-0040. The authors would like to thank D. Kleponis, E. Horwath, P. Patel, B. Scott and B. Vonk for their helpful discussions and support throughout this effort.

References

1. S.P. Marsh, *LASL Shock Hugoniot Data* (University of California Press, CA, 1980), p. 446
2. Y.M. Gupta, J. Appl. Phys. **51**, 5352 (1980)
3. M. Nasraoui, P. Forquin, L. Siad, A. Rusinek, Mater. Des. **37**, 500 (2012)
4. R. Quinson, J. Perez, M. Rink, A. Pavan, J. Mater. Sci. **32**, 1371 (1997)
5. N.A. Fleck, W.J. Stronge, J.H. Liu, Proc. R. Soc. Lond. A **429**, 459 (1990)
6. W.R. Blumenthal, C.M. Cady, M.F. Lopez, G.T. Gray III, D.J. Idar, *Shock Compression of Condensed Matter-2001* (American Institute of Physics, 2002), p. 665
7. Z. Li, J. Lambros, Int. J. Solids Struct. **38**, 3549 (2001)
8. A.D. Mulliken, M.C. Boyce, Int. J. Solids Struct. **43**, 1331 (2006)
9. J. Richeton, S. Ahzi, K.S. Vecchio, F.C. Jiang, R.R. Adharapurapu, Int. J. Solids Struct. **43**, (2006)
10. P. Moy, W. Chen, T. Weearsooriya, A. Hsieh, *Proceedings of the 2003 ASME Int. Mech. Eng. Congress* (Washington, DC, Nov. 2003)
11. D. Rittel, A. Brill, J. Mech. Phys. Solids **56**, 1401 (2008)
12. J.S. Harris, I.M. Ward, J.S.C. Parry, J. Mater. Sci. **6**, 110 (1971)
13. H. Wu, G. Ma, Y. Xia, Mater. Lett. **58**, 3681 (2004)
14. L.M. Barker, R.E. Hollenbach, J. Appl. Phys. **41**, 4208 (1970)
15. F.J. Zerilli, R.W. Armstrong, J. Mater. Sci. **42**, 4562 (2007)
16. D. Porter, P.J. Gould, Int. J. Solids, Struct. **46**, 1981 (2009)
17. T.J. Holmquist, G.R. Johnson, J. Phys. IV (France) **1**, 853 (1991)
18. G.R. Johnson, W.H. Cook, *Proceedings of the 7th International Symposium on Ballistics* (The Hague, Netherlands, 1983)
19. G.R. Johnson, R.A. Stryk, T.J. Holmquist, S.R. Beissel, Report No. WL-TR-1997-7039, Wright Laboratory (1997)
20. G.R. Johnson S. Chocron, C.E. Anderson, S.R. Beissel, T.J. Holmquist, *Proceedings of the 27th International Symposium on Ballistics* (Freiburg, Germany, 2013)
21. G.R. Johnson, W.H. Cook, Eng. Frac. Mech. **21**, 31 (1985)
22. A.J. Hsieh, D. DeSchepper, P. Moy, P.G. Dehmer, J.W. Song, Report No. ARL-TR-3155, Army Research Laboratory (2004)
23. P.G. Dehmer, M.A. Klusewitz, Report No. ARL-RP-45, Army Research Laboratory (2002)